Multiscale framework for estimation of elastic properties of Poly ethylene terephthalate from the crystallization temperature

Yun-Mei Luo [a], Fabrice Detrez [a], Luc Chevalier [a,*], Xiaoxin Lu [a,b], Sébastien Roland [b]

[a] Laboratoire Modélisation et Simulation Multi-Echelle, UMR 8208 CNRS, UNIVERSITÉ GUSTAVE EIFFEL, 5 Bd Descartes, 77454 Cedex 2, Marne-la-Vallée, France
[b] Laboratoire Procédés et Ingénierie en Mécanique et Matériaux, CNRS - UMR 8006, Arts et Métiers ParisTech, 151 bd de l'Hôpital, 75013, Paris, France

Keywords:
Spherulitic microstructure modelling
Poly ethylene terephthalate
Elastic properties prediction
Micromechanics homogeneization

A B S T R A C T

A 2D multiscale numerical strategy is presented in this paper. It allows to generate a representative elementary volume (REV) with a spherulitic microstructure used to predict the elastic properties of PET using a 2-scale numerical homogenization scheme. Because of the rapid crystallization kinetics of PET, DSC and optical microscopy were combined with empirical laws to estimate the crystallization kinetic parameters used to generate the REVs. Our framework allows estimating the elastic properties identified by tensile tests for several specimens crystallized at different temperatures. In addition, the comparison with mean-field models from the literature confirms that the Young's modulus of PET does not only depend on the crystallinity volume ratio but also on the crystal organization in the spherulites. The main advantage of this study is to provide a strategy for estimating the elastic properties that can be transposed to many semi-crystalline polymers with a spherulitic microstructure. Nevertheless, the numerical framework presented in the article is limited to semicrystalline polymers with a spherulitic microstructure, which crystallize under isothermal condition.

1. Introduction

Poly (ethylene terephthalate) (PET) is one of the most important commercial thermoplastic polymer because of its ability of being oriented and molded in different forms (Colomines et al., 2005). This material is widely used in industry and specifically in the production of packaging material (Chen et al., 2009; La Mantia et al., 2012; Haung et al., 2007; Billon et al., 2005; Menary et al., 2012; Luo et al., 2021; Schmidt et al., 1998). PET can exhibit different morphologies (purely amorphous or semi-crystalline showing spherulitic or shish-kebab morphologies) depending on the processing conditions. These types of microstructures have a strong influence on the physical and the mechanical properties (see, e.g. (Mandelkern, 2004; Reiter and Sommer, 2003; Piorkowska and Rutledge, 2013) for a comprehensive description of polymer crystallization). Therefore, the study of crystallization of the semi-crystalline polymer has gained increasing importance to the engineering in the past few years (Jabarin, 1984; Groeninckx et al., 1974; van Drongelen et al., 2016; Chevalier and Marco, 2007).

The purpose of this article is to predict the elastic constants of PET as a function of its isothermal crystallization temperature. The originalities of this study are, in one hand, to combine a numerical framework for generating a spherulitic microstructure (Lu et al., 2019) with a micromechanical model of spherulitic aggregate; in the other hand, to identify experimentally the kinetic parameters of crystallization of PET as function of crystallization temperature. Indeed, in the specific case of PET, this experimental study appears to be intricate for two major reasons: the high nucleation rate, which induces a crystallization onset before reaching the isothermal plateau; and the small size of the spherulites, which makes it difficult to assess their radii by optical microscopy. Despite these difficulties, some experimental studies have been carried out by differential scanning calorimetry (DSC) (Jabarin, 1987; Hieber, 1995), and by polarized light optical microscopy (Medellin-Rodriguez et al., 2000). We used a three-step approach. First, the crystallization parameters (the half-time of crystallization, $t_{1/2}$, the spherulite growth rate, G, and the crystallinity volume ratio, α_c) are estimated experimentally or using empirical laws for all studied annealing temperatures. Then, using the numerical framework of spherulitic microstructure generation (Lu et al., 2019), we built a 2D Representative Volume Element (RVE) for all annealing temperatures, which allowed us to estimate the elastic properties by numerical homogenization. Finally, we compared the estimates of this multiscale model to the experimental results from tensile tests and the mean-field

* Corresponding author.
E-mail addresses: yun-mei.luo@univ-eiffel.fr (Y.-M. Luo), fabrice.detrez@univ-eiffel.fr (F. Detrez), Luc.Chevalier@univ-eiffel.fr (L. Chevalier), luxiaoxin.cassie@gmail.com (X. Lu), Sebastien.roland@ensam.eu (S. Roland).

https://doi.org/10.1016/j.mechmat.2023.104617

homogenization approach of the literature.

One of the traditional ways of modelling the mechanical behavior of semi-crystalline polymers is the phenomenological approach, which associates the crystal and amorphous phase at different element rheology element (see, e.g. (Regrain et al., 2009; Detrez et al., 2010; Yan et al., 2021; Pedoto et al., 2021)). The other approaches, based on micromechanics, are divided into two families: the mean-field models, such as self-consistent model (Nikolov et al., 2002; Guan and Pitchumani, 2004; Bédoui et al., 2006; Gueguen et al., 2010), $\overline{\mathscr{U}}$-inclusion (Van Dommelen et al., 2003a; Mirkhalaf et al., 2019) and the full field models, where the effective properties are computed by numerical homogenization (Van Dommelen et al., 2003b; Michaeli et al., 2012; Oktay and Gürses, 2015; Laschet et al., 2017) on REV of the spherulitic microstructure. It is important to note than Teixeira-Pinto et al. have shown experimentally that a volume element with forty spherulites could be consider like an RVE for semi-crystalline polymers (Teixeira-Pinto et al., 2016). In the literature, several computer methods have been proposed to predict the crystallization kinetics and the morphology of semi-crystalline polymers. These include the level set method (Liu et al., 2015), the phase field method (Gránásy et al., 2005; Wang et al., 2013; Fang and Haataja, 2015; Gong et al., 2019), the pixel coloring method (Durin et al., 2015, 2017) from which the used method (Lu et al., 2019) is inspired, the cellular automaton method (Raabe, 2004; Raabe and Godara, 2005), the stochastic simulation (Micheletti and Burger, 2001; Capasso et al., 2003; Molnar et al., 2021), the Monte-Carlo method, and the raytracking method (Spina et al., 2014, 2016; Spekowius et al., 2016).

This article is organized as follows. section 2 contains the details on materials and experimental methods. Then, the following section provides the experimental characterization of crystallinity parameters and mechanical properties for several annealing temperatures. section 4 is dedicated to the presentation of the numerical framework that allows us to estimate the elastic properties from the annealing temperature. The reader will find there the details on the microstructure generator and on the strategy of numerical homogenization. Finally, in the last section, we discuss and compare the results of the proposed approach with the experimental results and the mean-field homogenization model of the literature.

2. Materials and methods

2.1. Material and sample preparation

The PET used in this study was provided by Polisan Hellas. The melting temperature was measured at about 240–250 °C. The recommended molding temperature is in the range 270–290 °C (Thompson and Woods, 1955). The average molecular weight *Mn* is 15,000 g/mol.

The PET square plates ($125mm \times 125mm$) with a thickness of 4 mm are injected at the PIMM laboratory. We cut the samples for tensile test and density measurements using the water jet-cutting machine ProtoMAX.

Due to the injection process condition, the plates were nearly amorphous. We assumed that the elastic properties (Young's modulus, $E_a = 2.10$ GPa, and Poisson's ratio, $\nu_a = 0.43$) and the mass density, $\rho_a = 1.33\ \mathrm{g/cm^3}$, measured from these plates are those of the amorphous phase. For sake of simplicity, we also neglected the property gradient sometimes observed on the injected parts. After sample cutting, annealing has been performed for 24 h in a Nabertherm oven to study the influence of the annealing temperature, T_a, on the mechanical properties and the crystallinity ratio. Eight different values of annealing temperature were selected 20 °C apart, between the glass transition temperature ($T_g \approx 90\,^\circ C$) and the melting temperature ($T_m^0 \approx 250\,^\circ C$ (Thompson and Woods, 1955)). All the specimens for tensile tests and density measurements have been placed inside the oven for over 24 h after temperature stabilization at given annealing temperature, T_a, to make sure that they were crystallized with similar microstructures. Note that no homogenization annealing above T_m^0 was carried out in order to erase the thermomechanical history induced by injection to avoid the crystallization during the cooling and to guarantee a controlled shape of our tensile specimens.

2.2. Density measurement

The crystallinity ratios have been characterized from a macroscopic point of view by density measurements. Distillated water with a few drops of wetting agent to remove air bubbles, was used and the temperature was carefully measured to consider the water density accurately for the density measurements of the PET samples.

Using the differential weight method, one weight in air and the other in water, the crystallinity ratio was calculated from the final density at different crystallization temperature. The volume crystallinity ratio α_c and the mass crystallinity ratio X_c are given by:

$$\alpha_c = \frac{\rho - \rho_a}{\rho_c - \rho_a}, \text{ and } X_c = \frac{\rho_c}{\rho}\alpha_c, \tag{1}$$

where ρ, ρ_c, ρ_a are respectively the specimen's density, the density of the PET crystal and the density of the amorphous phase. The reference densities are $\rho_a = 1.33\ \mathrm{g/cm^3}$, that is measured from the amorphous injected plate; and $\rho_c = 1.50\ \mathrm{g/cm^3}$, that is given in the literature (Thompson and Woods, 1955). Each density measurement was done five times and dispersion is less than 0.5%.

2.3. Tensile test

Four Dog-Bone test specimens (gage length 110 mm, gage width 8 mm and thickness 4 mm) were cut for each studied annealing temperature and for the amorphous PET. Tensile tests were conducted on an Instron uniaxial tensile machine at a traverse velocity of 0.5 mm/min (strain rate, $\dot{\varepsilon} \approx 7.6\ 10^{-5} s^{-1}$). From the strain-stress curve, the yield stress and the ultimate tensile strength were extracted. A speckle was painted on the specimen as shown on Fig. 1, and a digital image correlation software (VIC2D) was used to characterize accurately the Young's modulus, E, and the Poisson's ratio, ν.

2.4. Optical microscopy

The optical microscope used was a polarizing Nikon Eclipse LV100 equipped with a Nikon DS Digital Sight DS-Fi1 camera and a heating stage Linkam FTIR600. Observations were carried out with an ocular lens of 50 × on PET film with a thickness of 6 µm prepared with a Leica RM-2235 microtome. Films were sandwiched between two glass cover slips and they were first heated at 10 °C.min−1 from room temperature

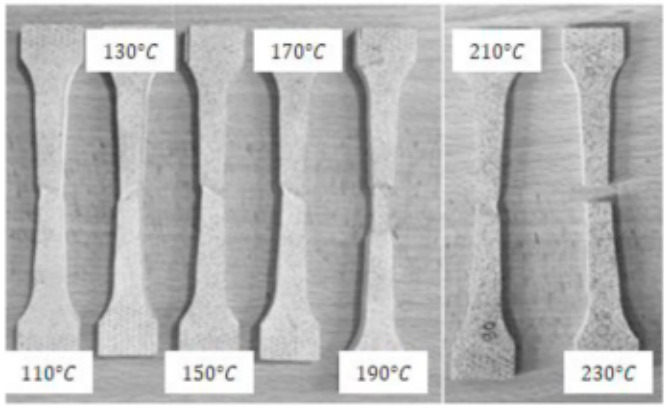

Fig. 1. Picture of tensile specimens after the yield point for all annealing temperatures.

to 280 °C during 5 min to erase the thermal history of the specimen. Then, it was cooled down at 40 °C.min−1 to 230 °C and maintained at this temperature during 30 min. This annealing temperature corresponds to the lowest supercooling, i.e. to the lowest nucleation rate allowing the formation of large spherulites. The radii of a dozen spherulites were measured as function time to evaluate the growth rate of spherulite, G.

2.5. Differential scanning calorimetry

Crystallization analyses were carried out in a TA Instruments Q1000 on samples of about 4–6 mg, which were cut from the injected plates. All specimens were first heated at 10 °C.min^{-1} from room temperature to 280 °C during 5 min. This temperature is above the PET melting temperature ($T_m^0 = 250°C$ (Thompson and Woods, 1955)) to erase the thermal history. For the study of kinetics of crystallization, samples were crystallized from the melt. The specimens were cooled at 30 °C.min^{-1} to the selected annealing temperatures (230 °C, 210 °C, and 190 °C) and maintained at this temperature during 24 h. Finally, they were cooled to room temperature at 30 °C.min^{-1}. For the annealing temperature bellow 190 °C, the PET used in this study crystallizes during the cooling ramp, that is why a non-isothermal analysis was used to estimate the half time of crystallization for the other annealing temperatures. For this constant cooling rate analysis, a cooling ramp at 30 °C.min^{-1} was performed from 280 °C to 110 °C.

3. Experimental results

3.1. Estimation of crystallization parameters

3.1.1. Growth rate of spherulite G

For all studied annealing temperatures, the growth rate of spherulite, G, have been estimated by the empiric model of van Antwerpen and van Krevelen (Van Antwerpen and Van Krevelen, 1972; Tant and Culberson, 1993)

$$\ln G(T) = \ln\left(\frac{2.93\times10^{14}}{M_n} - 5\times10^{9}\right) - \frac{777}{T-316} - \frac{3093\times10^{5}}{T^2(573-T)}, \tag{2}$$

where $M_n = 15000$ g/mol is the average molecular weight of the studied PET. The optical result is limited to 2D observations on thin films. The thickness of the film can influence the crystallization kinetics, in particular, the nucleation rate I but, also, the growth rate G. However, Arzilli et al. observed that the growth rates of the lamellae (10−6–10−7 cm/s) in spherulites are either similar or slightly higher than for 3D single crystals (Arzilli et al., 2015). Consequently, we used the microscopic measurement to adjust the model used to calculate G (Eq. (2)).

Table 1 provides the growth rate as well as the volume crystallinity ratio α_c for all annealing temperatures. Moreover, Table 1 gives the experimental value of growth rate obtained by optical microscopy for the isothermal crystallization at the annealing temperature $T_a = 230\,°C$. This value $G = 6.3\text{x}10^{-3}$ µm/s are in accordance with the model of Equation (2). Fig. 2 shows the micrographs of the crystallization process. Small spherulites begin to appear at time $t = 9$ min. After 17 min, one can see that the spherulites have grown. The mean radius of spherulite from the final micrograph is about 10 µm. Furthermore, Fig. 3 shows the linearity of the evolution, versus the time, of the radii (R_i) of two spherulites S1 and S2 followed during the same crystallization. The growth rate of spherulite is characterized by the average of slope over a dozen of spherulites.

3.1.2. Estimation of the half-time of crystallization $t_{1/2}$

For temperature between 190 °C and 230 °C, the identification of the parameters of the Avrami's model has been done from isothermal DSC analysis by estimating the relative crystallinity, $\chi(t) = X_c(t)/X_c^{\infty}$, where $X_c(t)$ is the instantaneous mass crystallinity ratio and X_c^{∞} is the ultimate mass crystallinity ratio. Fig. 4a shows a very good agreement between the experimental results and the Avrami's model for the 220 °C case. Fig. 4a shows the Avrami's plot for temperatures from 190 °C to 230 °C.

For temperature below 190 °C, the crystallization is too fast to perform classic isotherm analysis. For this reason, isokinetics DSC analysis was used at constant cooling rate of −30 °C/min. To perform the identification, the differential form of the Avrami's model, so called Nakamura's model, was used (Nakamura et al., 1973; Eder, 1997):

$$\dot{\chi} = n(T)K(T)(1-\chi)\left(\frac{\ln((1-\chi))}{K(T)}\right)^{\frac{n(T)-1}{n(T)}} \tag{3}$$

where $K(T)$ and $n(T)$ are the Avrami's constant and exponent at constant temperature T. Following Hieber's work (Hieber, 1995), a quadratic form was assumed for the logarithm of Avrami's constant, i.e. $\log(K(T)) = aT^2 + bT + c$. Moreover, a spontaneous nucleation was assumed, i.e. the Avrami's exponent $n(T) = 3$ for all temperatures. The three constants a, b, and c were fitted by minimizing the error, in the least-squares sense, between the experimental result and the prediction of Nakamura's model Eq. (3). *In fine*, this approximation of Avrami's constant was used as a function of temperature to estimate the half-time of crystallization $t_{1/2}$.

$$t_{1/2} = \left(\frac{\ln 2}{K(T)}\right)^{\frac{1}{3}}. \tag{4}$$

Table 1 provides the estimations of half-time of crystallization $t_{1/2}$ for all annealing temperatures and the experimental values for the temperatures from 190 °C to 230 °C. Indeed, for these temperatures, it was possible to perform isotherm analysis. Fig. 4b shows a very good agreement with the experimental results and the Nakamura's model, as it can be shown for 190 °C and 230 °C.

Hieber (1995) summarized all constant cooling rate or isothermal DSC on PET in a graph introducing the parameter $\lambda(T)$ that is proportional to $t_{1/2}$:

$$\lambda(T) = \frac{t_{1/2}}{(\ln 2)^{\frac{1}{3}}} \tag{5}$$

Fig. 5 compares the λ(T) values obtained from our incremental identification with the Hieber's mean parabola obtained from numerous references. Some differences occur when approaching glass transition and melt temperature or near the maximum crystallization temperature 170 °C. Nevertheless, considering the important dispersion associated to this mean parabola, the agreement is good between the literature results and our identification. The values of t1/2 of Table 1 will be used in the following to estimate the kinetics of the spherulite growth.

Table 1
Crystallization parameters as a function of annealing temperature T_a where α_c is the volume crystallinity ratio α_c, G is growth rate of spherulite, and $t_{1/2}$ is the half-time of crystallization.

T_a [°C]		110	130	150	170	190	210	230
α_c [−]		18.5%	19,5%	24%	27%	36%	44%	54%
G [µm/s]	Exp.	–	–	–	–	–	–	6.3×10^{-3}
	Eq. (2)	2.1×10^{-3}	2.7×10^{-2}	1.1×10^{-1}	1.8×10^{-1}	1.5×10^{-1}	5.8×10^{-2}	6.2×10^{-3}
$t_{1/2}$ [min]	Exp	–	–	–	–	8.1×10^{-1}	4.25	$5.0\times10^{+01}$
	Eq. (4)	$3.8\times10^{+02}$	$1.2\times10^{+01}$	1.36	5.6×10^{-01}	8.2×10^{-01}	4.34	$5.3\times10^{+01}$

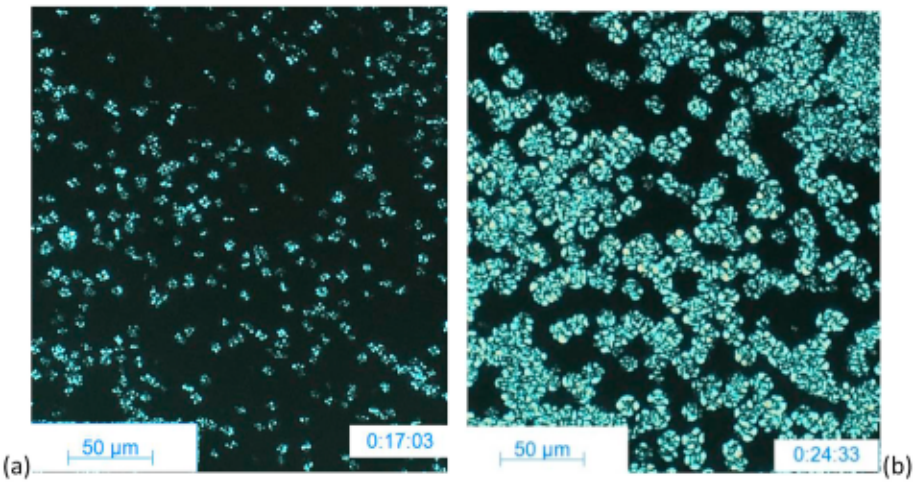

Fig. 2. Optical microscope: PET spherulites during crystallization at 230 °C (a) at 17 min; (b) at 24 min..

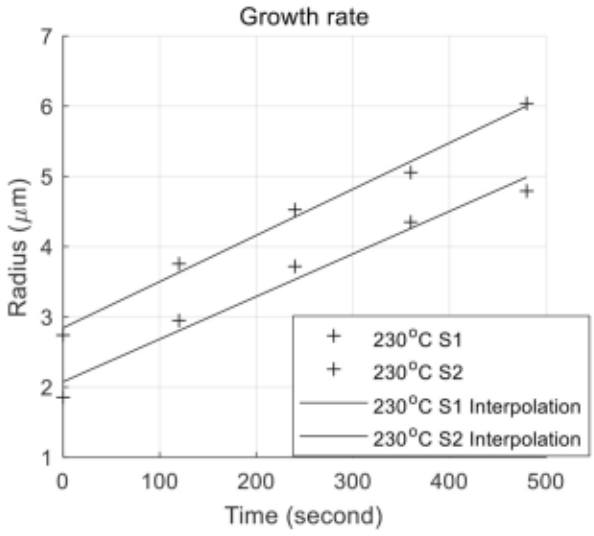

Fig. 3. Evaluation of the growth rate of spherulite G at 230 °C from radius evolution.

3.2. Characterization of annealing specimens

From the strain-stress curve, the yield stress, σ_Y, and the ultimate tensile strain (UTS) were measured. In order to characterize accurately the Young's modulus and the Poisson's ratio , a digital image correlation technique was used. Fig. 6 shows the evolution of these material parameters as a function of the annealing temperature.

These graphs (Fig. 6) and the picture (Fig. 1) also highlight the different behaviors that vary from ductile at low temperature to brittle when annealing temperature increases.

With the highest studied temperature, the specimen becomes more rigid and brittle. For the specimen heated at 230 °C, the behavior was so brittle that only two tests were succeeded compared to the five specimens tested for all other temperatures. The yield stress σ_Y (Fig. 6b) and the ultimate tensile strain (Fig. 6c) vary the opposite way than the rigidity. Strength variation is not significant from 90 to 170 °C, and then decreases quickly. The failure elongation decreases regularly. That confirms the material becomes brittle. Regarding the Young's modulus from Fig. 6a, the more the material is heated, the higher the Young's modulus while the Poisson's ratio remains almost constant. This increasing evolution is quite similar to the evolution of the volume crystallinity ratio α_c (see Table 1). Similar behavior has been already observed in the case of polybutene in the literature (Thomas et al., 2009). It was interpreted as caused by the increase of the lamellae thickness as well as the crystallization ratio when crystallization temperature increases.

4. Multiscale modelling

In this section, we present our numerical framework to estimate the elastic properties of PET as function of the annealing temperature. Only optical microscopy was 2D because of the small thickness but these measures were not used to determine I, which could be obtained from the DSC measurements via Eq. (8). Consequently, all measurements are 3D but for the sake of simplicity, and because results are satisfactory, we managed a 2D mechanical analysis. Our multiscale approach is a two steps homogenization: first the homogenization of multilayer stack of crystal and amorphous phase, then the numerical homogenization on a 2D REV of the spherulitic microstructure (see Fig. 7). For the second step, the elastic properties depend on the orientation of crystalline lamellae, θ_c. We start this section by the explanation of the generator of 2D REV.

4.1. REV generator

The generator of spherulitic microstructure is based on a nucleation and growth process on a pixelated grid ($S_0 = D \times D$) (Lu et al., 2019). The pixels have the dimension $\Delta x = D/150$. The inputs of this generator are the rate of nucleation I and the growth rate G. The growth of spherulites can be expressed in a simple way:

$$R_i(t) = G\langle t - \frac{i}{IS_0}\rangle_+ \tag{6}$$

where $R_i(t)$ gives the radius evolution of the of the ith spherulite in the REV at time t. Each new nucleus "i" appears at $t_i = i/IS_0$. Its location (x_i, y_i) is randomly chosen inside the non-crystalized part surface S_0 of the REV. Symbol $\langle t - t_i\rangle_+$ corresponds to the positive part of t - t_i. This gives the evolution of the reduced volume crystalline phase area at time t until no coalescence occurs between spherulites:

$$\chi_c = \frac{S_c}{S_0} = \frac{\pi G^2 \sum_{i=1}^{N(t)} \langle t - \frac{i}{IS_0}\rangle^2}{S_0} \tag{7}$$

Equation (7) shows that when χ_c is close to 1, the term $G^2/(I^2.S_0^2)$ has the same order of magnitude than S_0. Consequently, a reasonable number of germs can be obtained and adjusted from a simulation to another by considering the characteristic length $L_c = G^{\frac{1}{3}}I^{-\frac{1}{3}}$ and by

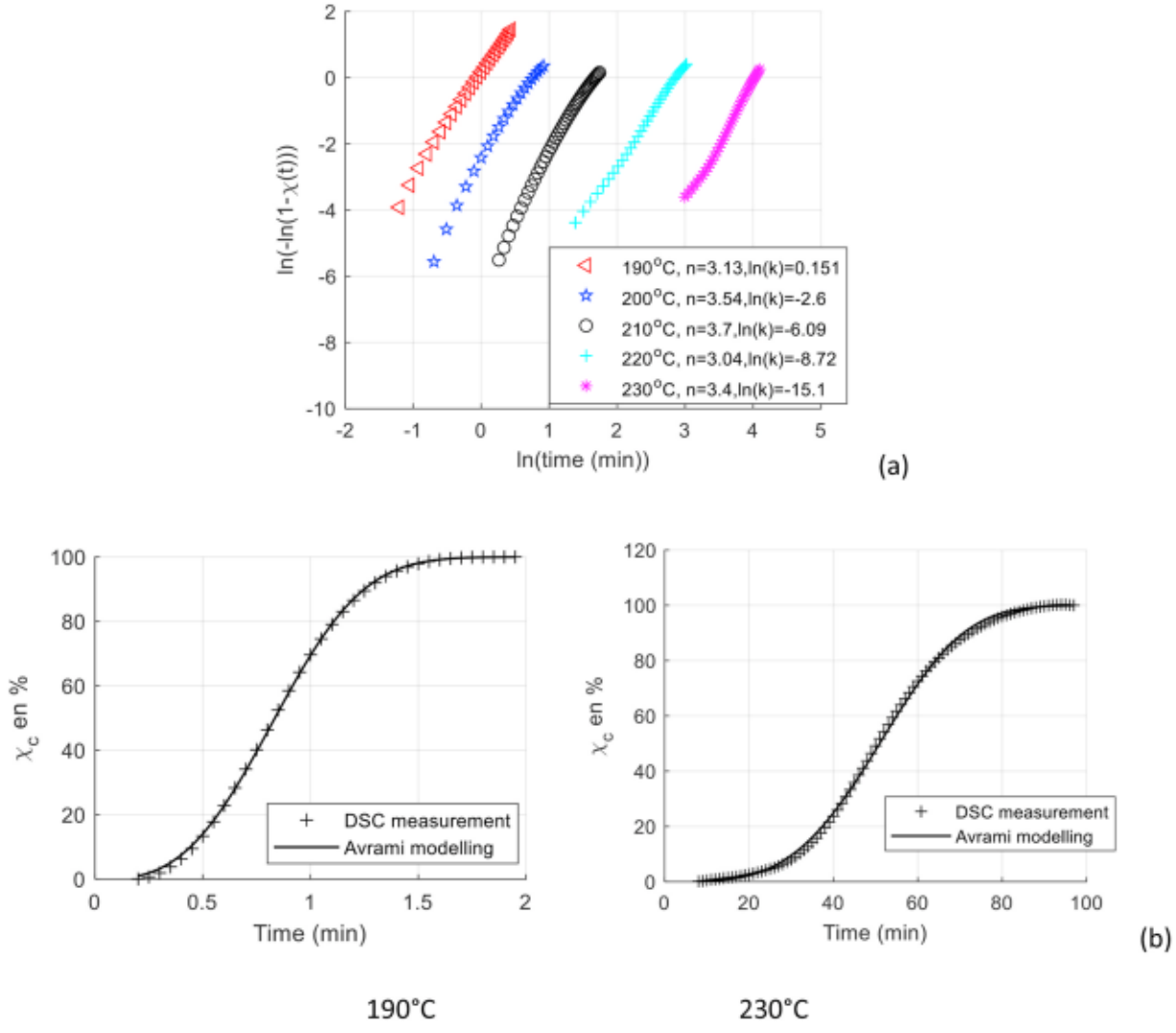

Fig. 4. (a) Avrami's plot for DSC measurements with temperature above and equal to 190 °C (b) Cristallization evolution compared from DSC measurements (dots) and modelling (line) with the interpolated Log (K(T)) function for 190 °C and 230 °C.

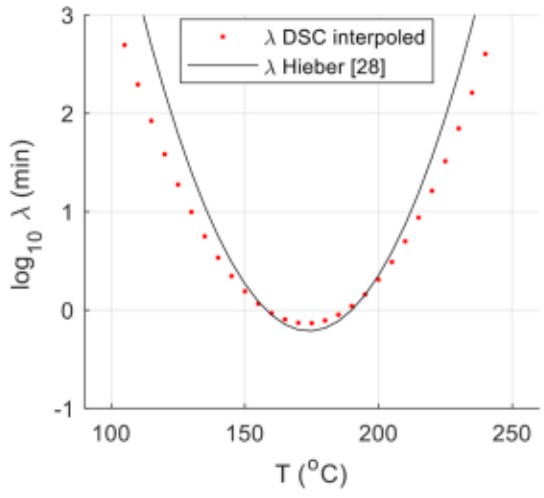

Fig. 5. Identification of Avrami's model: Comparison of λ(T) parabola with experimental curve from Hieber (Hieber, 1995).

choosing the dimension of the box proportional to this length by $D = k$. L_c. In order to have on average $N_{sph} = 85$ spherulites per trial of spherulitic microstructure, we choose $D = 10\ L_c$. Note that this number of spherulites is twice as large as the minimum number of spherulites needed to have a reliable REV, which was estimated experimentally by Teixeira et al. (Teixeira-Pinto et al., 2016).

The outputs of the generator are the spherulite distribution and the orientation field of the crystal lamellae, $\theta_c(x)$, at each point x. We assume that the lamella direction is equal to the angle between the vector $\boldsymbol{e}_1^{meso}$ and the vector from the spherulite nuclei of the i-th spherulite, $\boldsymbol{x}_0^{(i)}$, to the current point x inside the i-th spherulite (see Fig. 7). As a complementary parameter, we use the characteristic time, $t_c = G^{-\frac{2}{3}} I^{-\frac{1}{3}}$, introduced by Lu et al. (2019). This quantity, together with L_c, allows to estimate the spherulite number ($N_{sph} \approx 0.089\ S_0 L_c^{-2}$) inside the REV of surface S_0, and the crystallization half-time $t_{1/2} \approx 0.9 t_c$, in case of sporadic crystallization. It is noteworthy that the simulations are conducted in 2D. The I and G expressions given in Lu et al. (2019) must therefore be adapted:

$$L_c = \left(\frac{G}{I}\right)^{\frac{1}{d+1}}, t_c = \left(G^d I\right)^{\frac{-1}{d+1}} \tag{8}$$

Where the exponent d gives the space dimension. In our case, we used d

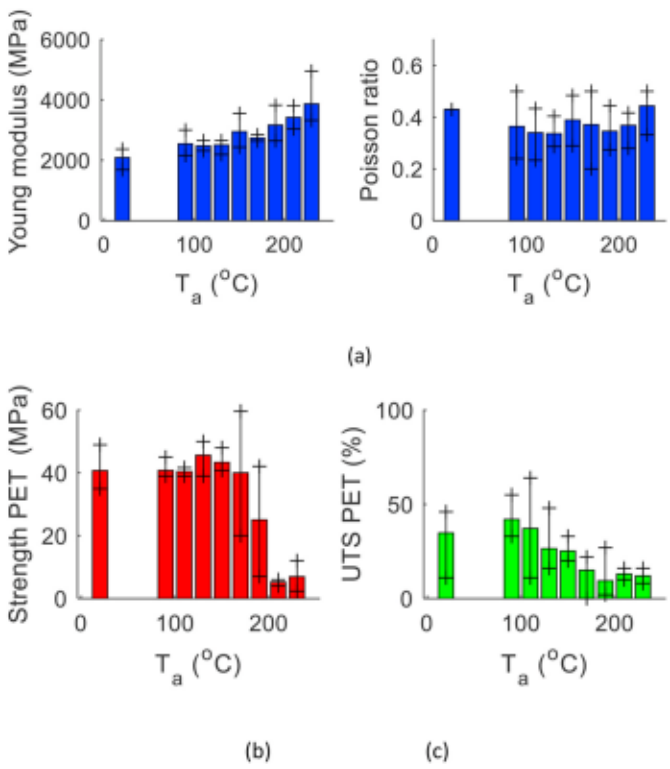

Fig. 6. (a) Young's modulus (left) and Poisson's ratio (right) of PET VS Temperature; (b) Strength of PET VS Temperature; (c) Strain at break VS Temperature.

$= 2$, while for 3D modelling of the crystallization kinetics, $d = 3$ must be used. Therefore, the relationship between t_c and $t_{1/2}$, combined with the knowledge of the growth rate G, gives the nucleation rate I for each annealing temperature T_a:

$$I = G^{-2} t_c^{-3} \approx 0.73 G^{-2} t_{1/2}^{-3} . \tag{9}$$

Fig. 8 shows a typical realization of microstructure for the annealing temperature $T_a = 210\,°C$. Table 2 gives the values used for each annealing temperature.

4.2. Mechanical properties prediction

In the next subsection, a two steps homogenization is conducted: first, to characterize the semi-crystalline lamellae behavior, second to characterize the behavior of the spherulitic morphology.

4.2.1. Notations

We use 2D modelling. We choose as notation lowercase bold letters for vectors (e.g. $\boldsymbol{e}_1, \boldsymbol{e}_2, \boldsymbol{n}$); bold Greek symbols for 2nd order tensors and components (e.g. $\boldsymbol{\sigma}, \boldsymbol{\varepsilon}$) and blackboard bold capital letter for 4th order tensors and components (e.g. $\mathbb{C}, \mathbb{S}$). We use Voigt's notations for the symmetric 2nd order tensors such that

$$[\sigma]_{\mathfrak{B}} = \begin{bmatrix} \sigma_1 = \boldsymbol{\sigma}_{11} \\ \sigma_2 = \boldsymbol{\sigma}_{22} \\ \sigma_3 = \boldsymbol{\sigma}_{12} \end{bmatrix}_{\mathfrak{B}} , [\varepsilon]_{\mathfrak{B}} = \begin{bmatrix} \varepsilon_1 = \boldsymbol{\varepsilon}_{11} \\ \varepsilon_2 = \boldsymbol{\varepsilon}_{11} \\ \varepsilon_3 = 2\boldsymbol{\varepsilon}_{12} \end{bmatrix}_{\mathfrak{B}} \tag{10}$$

where $\mathfrak{B} = (\boldsymbol{e}_1, \boldsymbol{e}_2)$ refers to the basis used to express the component $\boldsymbol{\sigma}_{ij}$ (resp. $\boldsymbol{\varepsilon}_{ij}$) of the stress tensor (resp. The strain tensor). With these notations the 4th order tensors of stiffness, $[\mathbb{C}]_{\mathfrak{B}}$, and compliance $[\mathbb{S}]_{\mathfrak{B}} = [\mathbb{C}]_{\mathfrak{B}}^{-1}$ are written as

$$[\mathbb{C}]_{\mathfrak{B}} = \begin{bmatrix} C_{11} & C_{12} & C_{31} \\ C_{12} & C_{22} & C_{23} \\ C_{31} & C_{23} & C_{33} \end{bmatrix}_{\mathfrak{B}} = \begin{bmatrix} \mathbb{C}_{1111} & \mathbb{C}_{1122} & \mathbb{C}_{1211} \\ \mathbb{C}_{1122} & \mathbb{C}_{2222} & \mathbb{C}_{2212} \\ \mathbb{C}_{1211} & \mathbb{C}_{2212} & \mathbb{C}_{1212} \end{bmatrix}_{\mathfrak{B}} \tag{11}$$

$$[\mathbb{S}]_{\mathfrak{B}} = \begin{bmatrix} S_{11} & S_{12} & S_{31} \\ S_{12} & S_{22} & S_{23} \\ S_{31} & S_{23} & S_{33} \end{bmatrix}_{\mathfrak{B}} = \begin{bmatrix} \mathbb{S}_{1111} & \mathbb{S}_{1122} & 2\mathbb{S}_{1211} \\ \mathbb{S}_{1122} & \mathbb{S}_{2222} & 2\mathbb{S}_{2212} \\ 2\mathbb{S}_{1211} & 2\mathbb{S}_{2212} & 4\mathbb{S}_{1212} \end{bmatrix}_{\mathfrak{B}} \tag{12}$$

We denote by $\mathscr{C}(\theta_c)$ the change-of-basis operator allowing to express the stiffness tensor in the basis $\mathfrak{B}_{meso}$, *i.e.* $[\mathbb{C}]_{\mathfrak{B}_{meso}} = \mathscr{C}(\theta_c) \star [\mathbb{C}]_{\mathfrak{B}_{micro}}$ as function of its expression in the basis $\mathfrak{B}_{micro}$. It is expressed in index notation with Einstein summation convention by

$$\mathbb{C}_{ijkl}^{\mathfrak{B}_{meso}} = \mathbb{C}_{pqrs}^{\mathfrak{B}_{micro}} Q_{pi} Q_{qj} Q_{rk} Q_{sl} \tag{13}$$

where Q is the change-of-basis matrix such as $\boldsymbol{e}_p^{micro} = Q_{pi}\, \boldsymbol{e}_i^{meso}$ and which is expressed in matrix notation by

$$Q = \begin{bmatrix} \cos(\theta_c) & \sin(\theta_c) \\ -\sin(\theta_c) & \cos(\theta_c) \end{bmatrix}. \tag{14}$$

where θ_c is the oriented angle from $\boldsymbol{e}_1^{meso}$ to $\boldsymbol{e}_1^{micro}$ (see Fig. 7).

We designate by $\langle\cdot\rangle_{sph}$ (resp. $\langle\cdot\rangle_{lam}$) the averaging operators which gives the macroscopic field (resp. The effective field of the lamellar stack) defined by

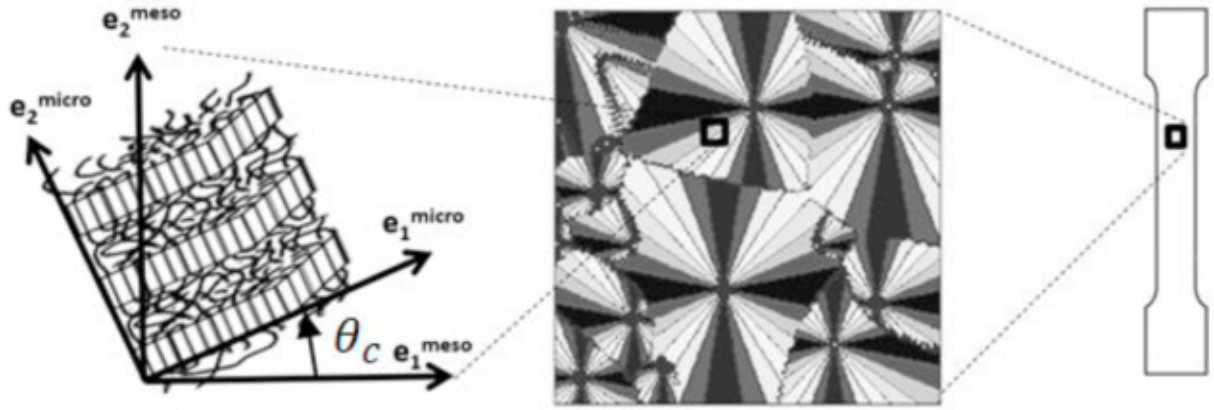

Fig. 7. Scheme of the two steps homogenization procedure. The contrast on 2D REV of spherulitic microstructure is due to the orientation of crystal lamellae (θ_c between 0 and $\frac{\pi}{2}$) to obtain a scheme similar to the picture from polarized light optical microscopy.

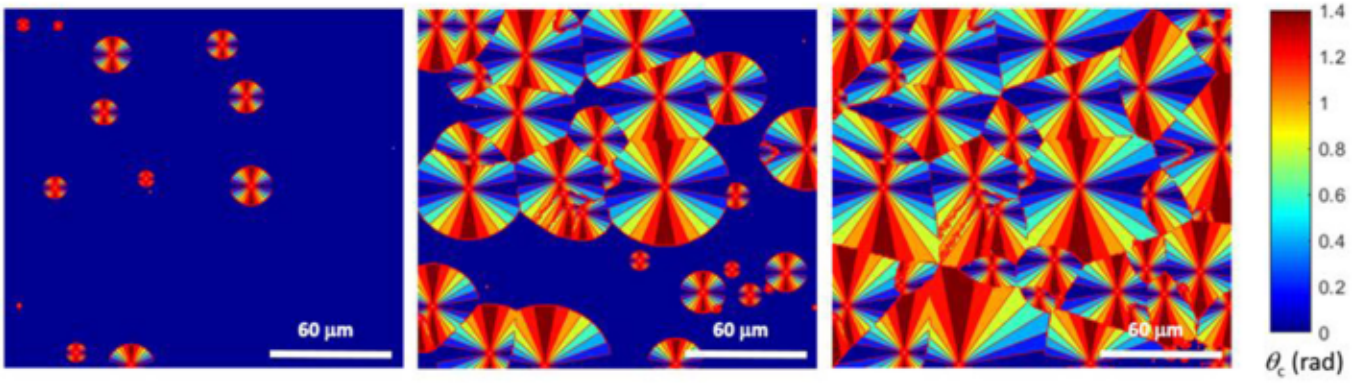

Fig. 8. Microscopic simulation: growth of spherulites until the final morphology of the crystal (length in µm).

Table 2
Input parameters of microstructure generator for all annealing temperatures.

T_a [°C]	110	130	150	170	190	210	230
$G[\mu m.s^{-1}]$	2.1 × 10^{-3}	2.7 × 10^{-2}	1.1 × 10^{-1}	1.8 × 10^{-1}	1.5 × 10^{-1}	5.8 × 10^{-2}	6.2 × 10^{-3}
$t_{1/2}[s]$	3.8 × 10^{+02}	1.2 × 10^{+01}	1.36	5.6 × 10^{-01}	8.2 × 10^{-01}	4.34	8.3 × 10^{+01}
I $[\mu m^{-2}.s^{-1}]$	1.5 × 10^{-8}	2.2 × 10^{-6}	2.1 × 10^{-5}	2.3 × 10^{-5}	2. x10^{-5}	6.7 × 10^{-6}	1.6 × 10^{-7}
L_c [µm]	51,9	23,1	17,4	19,8	19,6	20,5	33,8

$$\langle\cdot\rangle_{sph} = \frac{1}{|\Omega_{sph}|}\int_{\Omega_{sph}} \cdot d\Omega \quad \text{and} \quad \langle\cdot\rangle_{lam} = \frac{1}{|\Omega_{lam}|}\int_{\Omega_{lam}} \cdot d\Omega \tag{15}$$

where Ω_{sph} denotes the REV at the spherulitic scale and Ω_{lam} the REV at the lamellar scale.

4.2.2. *First step: homogenization of a semi-crystalline lamella*

We assume that the microstructure of a semi-crystalline polymer consists of an infinite stack of amorphous layer and crystalline lamella at the scale of crystallite. Considering the 2D mechanical analysis, we choose to quantify the rigidity matrix of both amorphous and crystal phase by taking directly the values of the Young's modulus and Poisson's ratio from the 3D behavior. We managed the 2D homogenization of the lamellae by taking the terms of the 3D analytical C matrix. The elastic behavior of the amorphous phase is assumed to be isotropic with Young's modulus $E_a = 2.10$ GPa and Poisson's ratio $\nu_a = 0.43$, and the crystal is assumed to be orthotropic, and that the macromolecular chains (the c axis of the crystal) are perpendicular to the interface amorphous crystal. The stiffness tensor of the amorphous phase and the crystal are in Voigt's notation:

$$[\mathbb{C}^a] = \begin{bmatrix} 3.24 & 1.39 & 0 \\ 1.39 & 3.24 & 0 \\ 0 & 0 & 1.85 \end{bmatrix}_{\mathfrak{B}_{micro}} \text{(GPa)}, \text{and } [\mathbb{C}^c] = \begin{bmatrix} 7.70 & 5.07 & 0 \\ 5.07 & 118 & 0 \\ 0 & 0 & 1.62 \end{bmatrix}_{\mathfrak{B}_{micro}} \text{(GPa)}. \tag{16}$$

Here, the properties of the amorphous phase come from the tensile tests on the amorphous injected plates ($C^a_{11} = C^a_{22} = E_a/(1-\nu_a^2)$, $C^a_{12} = E_a\nu_a/(1-\nu_a^2)$ and $C^a_{33} = E_a/2(1+\nu_a)$) and the properties of the crystal comes from the literature (Bédoui et al., 2006).

In this kind of infinite stratified microstructures, it can be shown that the stress and strain fields are constant per phase (Milton, 2002). Consequently, the effective stress tensor $\boldsymbol{\sigma}^{hi} = \langle\boldsymbol{\sigma}\rangle_{lam}$ and effective strain tensor $\boldsymbol{\varepsilon}^{hi} = \langle\boldsymbol{\varepsilon}\rangle_{lam}$ at the lamellar scale verifies the following mixing laws

$$\boldsymbol{\sigma}^{hi} = \langle\boldsymbol{\sigma}\rangle_{lam} = \alpha_c\boldsymbol{\sigma}^c + (1-\alpha_c)\boldsymbol{\sigma}^a \tag{17}$$

$$\boldsymbol{\varepsilon}^{hi} = \langle\boldsymbol{\varepsilon}\rangle_{lam} = \alpha_c\boldsymbol{\varepsilon}^c + (1-\alpha_c)\boldsymbol{\varepsilon}^a \tag{18}$$

where $\boldsymbol{\sigma}^a$ et $\boldsymbol{\sigma}^c$ (resp. $\boldsymbol{\varepsilon}^a$ et $\boldsymbol{\varepsilon}^c$) are the stress tensor (resp. The strain tensor) inside the amorphous layer and inside the crystal lamellae.

In addition, the stress must satisfy the continuity of traction vector across the interface between crystal and amorphous phase (mutual action principle)

$$\boldsymbol{\sigma}^{hi}.\boldsymbol{e}_2^{micro} = \boldsymbol{\sigma}^c.\boldsymbol{e}_2^{micro} = \boldsymbol{\sigma}^a.\boldsymbol{e}_2^{micro} \tag{19}$$

And the perfect adhesion between phases implies the strain compatibility in the interface plan. This writes

$$\boldsymbol{e}_1^{micro}.\left(\boldsymbol{\varepsilon}^{hi}.\boldsymbol{e}_1^{micro}\right) = \boldsymbol{e}_1^{micro}.\left(\boldsymbol{\varepsilon}^c.\boldsymbol{e}_1^{micro}\right) = \boldsymbol{e}_1^{micro}.\left(\boldsymbol{\varepsilon}^a.\boldsymbol{e}_1^{micro}\right) \tag{20}$$

By combining these relations with the linear elastic constitutive laws of the two phases, we obtain that the effective behavior is orthotropic. It is defined by the stiffness matrix $[\mathbb{C}^{hi}]_{\mathfrak{B}_{micro}}$.

$$[\mathbb{C}^{hi}]_{\mathfrak{B}_{micro}} = \begin{bmatrix} C_{11}^{hi} & C_{12}^{hi} & 0 \\ C_{12}^{hi} & C_{22}^{hi} & 0 \\ 0 & 0 & C_{33}^{hi} \end{bmatrix}_{\mathfrak{B}_{micro}}. \tag{21}$$

with

$$C_{11}^{hi} = \langle C_{11}\rangle_{lam} + \langle\frac{C_{12}}{C_{22}}\rangle_{lam}^2\langle\frac{1}{C_{22}}\rangle_{lam}^{-1} - \langle\frac{(C_{12})^2}{C_{22}}\rangle_{lam} \tag{22}$$

$$C_{22}^{hi} = \langle\frac{1}{C_{22}}\rangle_{lam}^{-1} \tag{23}$$

$$C_{33}^{hi} = \langle\frac{1}{C_{33}}\rangle_{lam}^{-1}, \tag{24}$$

$$C_{12}^{hi} = \langle\frac{C_{12}}{C_{22}}\rangle_{lam}\langle\frac{1}{C_{22}}\rangle_{lam}^{-1} \tag{25}$$

where $\langle C_{ij}\rangle_{lam} = \frac{1}{|\Omega_{lam}|}\int_{\Omega_{lam}} C_{ij}(x)\, d\Omega = \alpha_c C_{ij}^c + (1-\alpha_c)C_{ij}^a$. The details of the calculation are given in supplementary information. Fig. 9 shows the evolution of the elastic constants as a function of volume crystallinity ratio α_c.

4.2.3. *Second step: homogenization of a spherulitic morphology*

To manage this second step of homogenization framework, finite element simulations are performed using kinematic uniform boundary conditions (KUBC) (see e.g. (Yvonnet, 2019) for a review of numerical

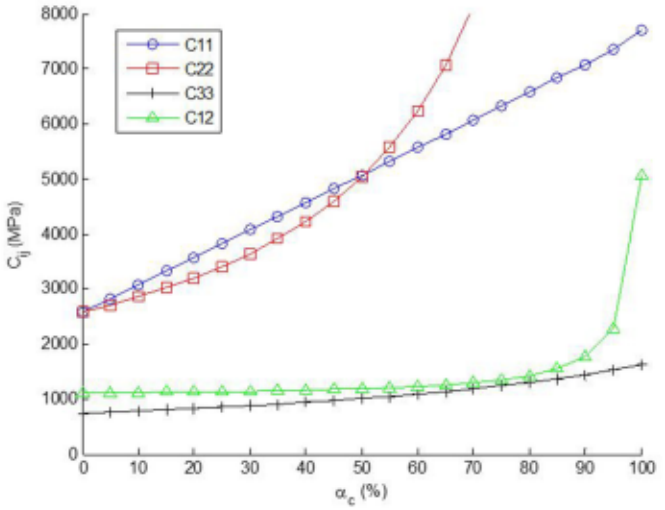

Fig. 9. Effective stiffness C_{ij}^{hi} of crystal amorphous stacks in basis $\mathfrak{B}_{micro}$ as a function of volume crystallinity ratio α_c.

homogenization). In this homogenization step the radial distribution of lamellae is supposed to be continuous. We make the assumption of scale separation. We take into account inside each spherulite, the orientation field of lamella, $\theta_c(\boldsymbol{x})$, is used to compute the local stiffness tensor $[\mathbb{C}(\boldsymbol{x})]_{\mathfrak{B}_{meso}} = \mathscr{C}(\theta_c(\boldsymbol{x})) \star [\mathbb{C}^{hi}]_{\mathfrak{B}_{micro}}$. The expression of stiffness tensor in the mesoscopic basis as function of lamellar writes

$$\mathrm{C}_{11}(\boldsymbol{x}) = C_{11}^{(hi)}(\cos(\theta_c))^4 + C_{22}^{(hi)}(\sin(\theta_c))^4 + \left(2C_{12}^{(hi)} + 4C_{33}^{(hi)}\right)(\cos(\theta_c)\sin(\theta_c))^2$$

$$\mathrm{C}_{22}(\boldsymbol{x}) = C_{11}^{(hi)}(\sin(\theta_c))^4 + C_{22}^{(hi)}(\cos(\theta_c))^4 + \left(2C_{12}^{(hi)} + 4C_{33}^{(hi)}\right)(\cos(\theta_c)\sin(\theta_c))^2$$

$$\mathrm{C}_{33}(\boldsymbol{x}) = \left(C_{11}^{(hi)} + C_{22}^{(hi)} - 2C_{12}^{(hi)}\right)(\cos(\theta_c)\sin(\theta_c))^2 + C_{33}^{(hi)}\left((\cos(\theta_c))^2 - (\sin(\theta_c))^2\right)^2$$

$$\mathrm{C}_{12}(\boldsymbol{x}) = \left(C_{11}^{(hi)} + C_{22}^{(hi)} - 4C_{33}^{(hi)}\right)(\cos(\theta_c)\sin(\theta_c))^2 + C_{12}^{(hi)}\left((\cos(\theta_c))^4 + (\sin(\theta_c))^4\right)$$

$$\mathrm{C}_{13}(\boldsymbol{x}) = \left(C_{11}^{(hi)} - C_{12}^{(hi)} - 2C_{33}^{(hi)}\right)(\cos(\theta_c))^3\sin(\theta_c) + \left(C_{12}^{(hi)} + 2C_{33}^{(hi)} - C_{22}^{(hi)}\right)\cos(\theta_c)(\sin(\theta_c))^3$$

$$\mathrm{C}_{23}(\boldsymbol{x}) = \left(C_{12}^{(hi)} + 2C_{33}^{(hi)} - C_{22}^{(hi)}\right)(cos(\theta_c))^3 sin(\theta_c) + \left(C_{11}^{(hi)} - C_{12}^{(hi)} - 2C_{33}^{(hi)}\right)cos(\theta_c)(sin(\theta_c))^3 \quad (26)$$

The classical numerical homogenization technique with a finite element calculation on the mesoscopic REV, Ω_{sph}, shown on the final image of Fig. 8 is managed. The REV is meshed with T3 finite elements based on the same grid used to generate the microstructure. We divide each pixel into two triangles. The procedure is achieved using KUBC method. The boundary conditions are

$$\boldsymbol{u}(\boldsymbol{x}) = \mathbf{E}\cdot(\boldsymbol{x} - \boldsymbol{x}_g) \forall \boldsymbol{x} \in \delta\Omega_{sph} \quad (27)$$

where $\mathbf{E}$ is the macroscopic strain tensor and $\boldsymbol{x}_g$ is the REV centroid. Under these boundary conditions, the mean stress and strain tensor are given by

$$\langle\boldsymbol{\varepsilon}\rangle_{sph} = \frac{1}{|\Omega_{sph}|}\int_{\Omega_{sph}} \boldsymbol{\varepsilon}\, d\Omega = \mathbf{E},\ \langle\boldsymbol{\sigma}\rangle_{sph} = \frac{1}{|\Omega_{sph}|}\int_{\Omega_{sph}} \boldsymbol{\sigma}\, d\Omega\,. \quad (28)$$

We impose three boundary conditions to estimate the effective stiffness tensor $\overline{\mathbb{C}}$: two elongations and one shear

$$\mathbf{E}^{(1)} = \begin{bmatrix} 1 & 0 \\ 0 & 0 \end{bmatrix}_{\mathfrak{B}_{micro}}, \mathbf{E}^{(2)} = \begin{bmatrix} 0 & 0 \\ 0 & 1 \end{bmatrix}_{\mathfrak{B}_{micro}}, \text{and} \quad \mathbf{E}^{(3)} = \frac{1}{2}\begin{bmatrix} 0 & 1 \\ 1 & 0 \end{bmatrix}_{\mathfrak{B}_{micro}}. \quad (29)$$

5. Results and discussion

For each annealing temperature, we conduct $n_t = 100$ simulations to perform statistical estimation of effective properties. We defined the statistical mean value, $E(\overline{C}_{ij})$, and standard deviation, $SD(\overline{C}_{ij})$, for the component of effective stiffness tensor $\overline{C}_{ij}$ by

$$E(\overline{C}_{ij}) = \frac{1}{n_t}\sum_{s=1}^{n_t}\overline{C}_{ij}^{(s)} \text{ and } SD(\overline{C}_{ij}) = \frac{1}{n_t - 1}\sum_{s=1}^{n_t}\left(\left(\overline{C}_{ij}^{(s)}\right)^2 - E(\overline{C}_{ij})^2\right) \quad (30)$$

where $\overline{C}_{ij}^{(s)}$ refers to the stiffness matrix component of s-th trial microstructure. We observe a good convergence of effective properties with a very small dispersion ($SD(\overline{C}_{ij})/E(\overline{C}_{ij}) < 1\%$) for all annealing temperature. The statistical average of stiffness tensor is closely isotropic because

$$\frac{|E(\overline{C}_{11}) - E(\overline{C}_{22})|}{E(\overline{C}_{11})} \leq 1\%, \frac{\left|E(\overline{C}_{33}) - \frac{1}{2}(E(\overline{C}_{11}) - E(\overline{C}_{12}))\right|}{E(\overline{C}_{33})} \leq 3\%$$

and $$\frac{|E(\overline{C}_{13})|}{E(\overline{C}_{11})} \approx \frac{|E(\overline{C}_{23})|}{E(\overline{C}_{11})} \leq 1\%\,.$$

We extract an estimation of Young's modulus, E^{macro}, and Poisson's ratios, ν^{macro}, from the statistical mean value of the effective stiffness tensor

$$E^{macro} = \frac{(E(\overline{C}_{11}) + E(\overline{C}_{22}))}{2}\left(1 - \frac{E(\overline{C}_{12})^2}{E(\overline{C}_{11})E(\overline{C}_{22})}\right), \nu^{macro} = \frac{1}{2}\left(\frac{E(\overline{C}_{12})}{E(\overline{C}_{11})} + \frac{E(\overline{C}_{21})}{E(\overline{C}_{22})}\right). \quad (31)$$

Fig. 10 shows the evolution of Young's modulus and Poisson's ratio as a function of volume crystallinity ratio. Our numerical two-step homogenization framework describes pretty well the evolution of experimental elastic properties. We also compared our framework with three mean field approaches (see e.g. (Chatzigeorgiou and Meraghni, 2022) for a review about these approaches): a Mori-Tanaka estimation and two self-consistent models. All the details of these models are given in the supplementary information. For these three approaches, we consider 210 crystal orientations, which are uniformly distributed. For sake of simplicity, we assume that the phase distribution is isotropic (i.e. the two-point correlation functions of phases probability depend only on the distance not on the direction (Torquato, 2002)). In Mori-Tanaka estimation and the first self-consistent estimation (SC1), we consider phases (amorphous phase and the crystalline orientation). For the second self-consistent estimation (SC2), we consider phases with the elastic properties from the homogenization of crystal amorphous multi-layer stack for each given crystalline orientation like Bédoui et al. (2006).

Our approach is qualitatively closer to the experimental results than the mean-field approaches (see Fig. 10). Indeed, the mean-field estimates are more compliant than both experimental results and our numerical homogenization framework. Furthermore, it is possible to stiffen these mean-field approaches by considering an ellipsoidal phase distribution (Guan and Pitchumani, 2004). This idea has been successfully used by Bédoui et al. to reproduce the experimental results with ellipsoidal inclusions, on PET and other usual semi-crystalline (Bédoui et al., 2006). In this study, the inclusion shape (i.e., the lamellae shape) ratios have been measured by X-ray diffraction (width/thickness = 2 and length/thickness = 2). Our approach, which explicitly takes into account the microstructure, makes it possible to overcome the

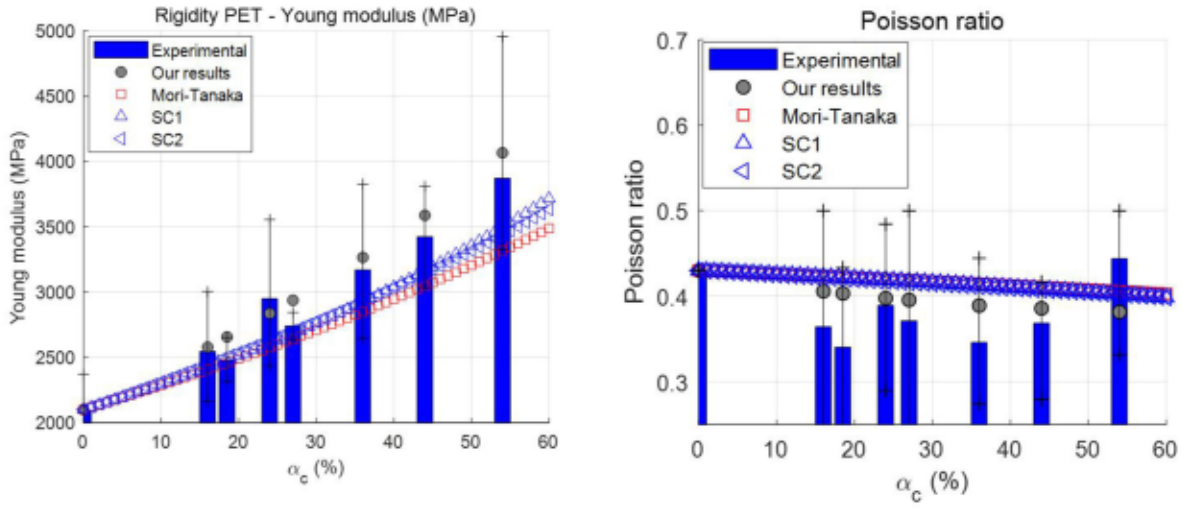

Fig. 10. Comparison between experiments and models: (left) Young's modulus as a function of volume crystallinity ratio α_c; (right) Poisson's ratio as a function of volume crystallinity ratio.

identification of the shape of the ellipsoid that may appear like fitting parameters.

6. Conclusions

In this paper, we have presented a numerical framework to estimate the elastic properties of PET using the crystallization temperature. The numerical strategy consists of one REV generator, with the half-time of crystallization $t_{1/2}$ and the spherulite growth rate G as input, and a two-step numerical homogenization procedure, *i.e.* at lamellar scale and at spherulitic scale. The estimation of kinetic properties of crystallization ($t_{1/2}$ and G) has been made jointly from empirical law Eq. (2) and Eq. (4), and DSC analysis and optical microscopy. Our model has provided an accurate estimation of elastic properties identified by tensile tests for all studied annealing temperatures. In addition, the comparison with mean-field homogenization models (Mori-Tanaka and Self-Consistent models) has confirmed that the Young's modulus of PET does not only depend on the crystallinity rate but also on the arrangement of the crystals in spherulites.

The main advantage of this study is to provide a strategy for estimating the elastic properties, which could be transposed to many semi-crystalline polymers with a spherulitic microstructure. The use of this approach on a polymer with a slower crystallization kinetics would be an interesting prospect to generate microstructures that are more realistic. A 3D modelling would also be an area for improvement. Nevertheless, with regard to the experimental dispersion on the Young's modulus and the Poisson's ratio, the 2D adopted model seems largely sufficient.

Credit author statement

Yun-Mei Luo: Conceptualization: Ideas; formulation or evolution of overarching research goals and aims, Methodology: Development or design of methodology; creation of models, Software: Programming, software development; designing computer programs; implementation of the computer code and supporting algorithms; testing of existing code components, Investigation: Conducting a research and investigation process, specifically performing the experiments, or data/evidence collection, Resources: Provision of study materials, reagents, materials, patients, laboratory samples, animals, instrumentation, computing resources, or other analysis tools, Writing - Original Draft: Preparation, creation and/or presentation of the published work, specifically writing the initial draft (including substantive translation), Visualization: Preparation, creation and/or presentation of the published work, specifically visualization/data presentation, **Fabrice Detrez**: Conceptualization: Ideas; formulation or evolution of overarching research goals and aims, Methodology: Development or design of methodology; creation of models, Software: Programming, software development; designing computer programs; implementation of the computer code and supporting algorithms; testing of existing code components, Validation: Verification, whether as a part of the activity or separate, of the overall replication/reproducibility of results/experiments and other research outputs, Formal analysis: Application of statistical, mathematical, computational, or other formal techniques to analyze or synthesize study data, Data Curation: Management activities to annotate (produce metadata), scrub data and maintain research data (including software code, where it is necessary for interpreting the data itself) for initial use and later reuse, Writing - Review & Editing: Preparation, creation and/or presentation of the published work by those from the original research group, specifically critical review, commentary or revision – including pre-or postpublication stages, Funding acquisition: Acquisition of the financial support for the project leading to this publication, **Luc Chevalier**: Conceptualization: Ideas; formulation or evolution of overarching research goals and aims, Methodology: Development or design of methodology; creation of models, Validation: Verification, whether as a part of the activity or separate, of the overall replication/reproducibility of results/experiments and other research outputs, Formal analysis: Application of statistical, mathematical, computational, or other formal techniques to analyze or synthesize study data, Resources: Provision of study materials, reagents, materials, patients, laboratory samples, animals, instrumentation, computing resources, or other analysis tools, Data Curation: Management activities to annotate (produce metadata), scrub data and maintain research data (including software code, where it is necessary for interpreting the data itself) for initial use and later reuse, Writing - Review & Editing: Preparation, creation and/or presentation of the published work by those from the original research group, specifically critical review, commentary or revision – including pre-or postpublication stages, Supervision: Oversight and leadership responsibility for the research activity planning and execution, including mentorship external to the core team, Project administration: Management and coordination responsibility for the research activity planning and execution, **Xiaoxin Lu**: Conceptualization: Ideas; formulation or evolution of overarching research goals and aims, Software: Programming, software development; designing computer programs; implementation of the computer code and supporting algorithms; testing of existing code components, Investigation:

Conducting a research and investigation process, specifically performing the experiments, or data/evidence collection, Resources: Provision of study materials, reagents, materials, patients, laboratory samples, animals, instrumentation, computing resources, or other analysis tools, **Sébastien Roland**: Validation: Verification, whether as a part of the activity or separate, of the overall replication/reproducibility of results/experiments and other research outputs, Resources: Provision of study materials, reagents, materials, patients, laboratory samples, animals, instrumentation, computing resources, or other analysis tools, Writing - Review & Editing: Preparation, creation and/or presentation of the published work by those from the original research group, specifically critical review, commentary or revision – including pre-or post-publication stages, Funding acquisition: Acquisition of the financial support for the project leading to this publication.

Declaration of competing interest

The authors declare that they have no known competing financial interests or personal relationships that could have appeared to influence the work reported in this paper.

Data availability

Data will be made available on request.

Acknowledgements

The authors thank the financial support of F2M (Fédération Francilienne de Mécanique, Coup de pouce 2017). The authors thank Professor Gilles Regnier and Paulo Ferreira for the injection of PET plates.

Appendix A. Supplementary data

Supplementary data to this article can be found online at https://doi.org/10.1016/j.mechmat.2023.104617.

References

Van Antwerpen, F., Van Krevelen, D.W., 1972. Influence of crystallization temperature, molecular weight, and additives on the crystallization Kinetics of Poly(ethylene terephthalate). J. Polym. Sci. 2423–2435. https://doi.org/10.1002/pol.1972.180101211.

Arzilli, F., Mancini, L., Voltolini, M., Cicconi, M.R., Mohammadi, S., Giuli, G., Mainprice, D., Paris, E., Barou, F., Carroll, M.R., 2015. Near-liquidus growth of feldspar spherulites in trachytic melts: 3D morphologies and implications in crystallization mechanisms. Lithos: An International Journal of Mineralogy, Petrology, and Geochemistry 216/217, 93–105. https://doi.org/10.1016/j.lithos.2014.12.003.

Bédoui, F., Diani, J., Régnier, G., Seiler, W., 2006. Micromechanical modeling of isotropic elastic behavior of semicrystalline polymers. Acta Mater. 54 (6), 1513–1523. https://doi.org/10.1016/j.actamat.2005.11.028.

Billon, N., Erner, A., Gorlier, E., 2005. Kinematics of Stretch Blow Moulding and Plug Assisted Thermoforming of Polymers; Experimental Study, vol. 21. Polymer Processing Society PPS, Leipzig, Germany.

Capasso, V., Burger, M., Micheletti, A., Salani, C., 2003. Mathematical models for polymer crystallization processes. In: Mathematical Modelling for Polymer Processing. Springer, Berlin, Heidelberg, pp. 167–242.

Chatzigeorgiou, G., Meraghni, F., 2022. N Charalambakis Multiscale Modeling Approaches for Composites. Elsevier. https://doi.org/10.1016/C2019-0-05214-4.

Chen, H., Pyda, M., Cebe, P., 2009. Non-isothermal crystallization of PET/PLA blends. Thermochim. Acta 492, 61–66. https://doi.org/10.1016/j.tca.2009.04.023.

Chevalier, L., Marco, Y., 2007. Identification of a strain induced crystallisation model for PET under uni- and bi-axial loading: influence of temperature dispersion. Mech. Mater. 39 (6), 596–609. https://doi.org/10.1016/j.mechmat.2006.09.001.

Colomines, G., Robin, J.-J., Tersac, G., 2005. Study of the glycolysis of PET by oligoesters. Polymer 46, 3230–3247. http://DOI:10.1016/j.polymer.2005.02.047.

Detrez, F., Cantournet, S., Seguela, R., 2010. A constitutive model for semi-crystalline polymer deformation involving lamellar fragmentation. Compt. Rendus Mec. 338 (12), 681–687. https://doi.org/10.1016/j.crme.2010.10.008.

Van Dommelen, J.V., Parks, D., Boyce, M., Brekelmans, W., Baaijens, F., 2003a. Micromechanical modeling of the elasto-viscoplastic behavior of semicrystalline polymers. J. Mech. Phys. Solid. 51 (3), 519–541. https://doi.org/10.1016/S0022-5096(02)00063-7.

Van Dommelen, J.A.W., Parks, D.M., Boyce, M.C., Brekelmans, W.A.M., Baaijens, F.P.T., 2003b. Micromechanical modeling of intraspherulitic deformation of semicrystalline polymers. Polymer 44 (19), 6089–6101. https://doi.org/10.1016/S0032-3861(03)00558-5.

van Drongelen, M., Roozemond, P.C., Peters, G.W., 2016. Non-isothermal crystallization of semi-crystalline polymers: the influence of cooling rate and pressure. In: Polymer Crystallization II. Springer, pp. 207–242. https://doi.org/10.1007/12_2015_344.

Durin, A., Chenot, J.-L., Haudin, J.-M., Boyard, N., L, J., 2015. Bailleul Simulating polymer crystallization in thin films: numerical and analytical methods. Eur. Polym. J. 73, 1–16. https://doi.org/10.1016/j.eurpolymj.2015.10.001.

Durin, A., Boyard, N., Bailleul, J.-L., Billon, N., Chenot, J.-L., Haudin, J.-M., 2017. Semianalytical models to predict the crystallization kinetics of thermoplastic fibrous composites. J. Appl. Polym. Sci. 134 (8) https://doi.org/10.1002/app.44508.

Eder, G., 1997. Mathematical modeling of crystallization processes as occurring in polymer processing. Nonlinear Anal. Theor. Methods Appl. 30, 3807–3815. https://doi.org/10.1016/S0362-546X(96)00231-3.

Fang, A., Haataja, M., 2015. Simulation study of twisted crystal growth in organic thin films. Phys. Rev. E 92 (4), 042404. https://doi.org/10.1103/PhysRevE.92.042404.

Gong, Y., Detrez, F., Luo, Y.M., Chevalier, L., 2019. Simulation of microstructure evolution for polymer using the phase field method: crystallization induced by temperature. Polymer Crystallization 2 (6). https://doi.org/10.1002/pcr2.10091.

Gránásy, L., Pusztai, T., Tegze, G., Warren, J.A., Douglas, J.F., 2005. Growth and form of spherulites. Phys. Rev. E 72 (1), 011605. https://doi.org/10.1103/PhysRevE.72.011605.

Groeninckx, G., Berghmans, H., Overbergh, N., Smets, G., 1974. Crystallization of poly (ethylene terephthalate) induced by inorganic compounds. I. crystallization behavior from the glassy state in a low-temperature region. J. Polym. Sci., Polym. Phys. Ed. 12, 303–316. https://doi.org/10.1002/pol.1974.180120207.

Guan, X., Pitchumani, R., 2004. A micromechanical model for the elastic properties of semicrystalline thermoplastic polymers. Polym. Eng. Sci. 44, 433–451. https://doi.org/10.1002/pen.20039, 3.

Gueguen, O., Ahzi, S., Makradi, A., Belouettar, S., 2010. A new three-phase model to estimate the effective elastic properties of semi-crystalline polymers: application to PET. Mech. Mater. 42 (1), 1–10. https://doi.org/10.1016/j.mechmat.2009.04.012.

Haung, H.X., Yin, Z.S., Liu, J.H., 2007. Visulisation study and analysis on preform growth in polyethylene terephthalate stretch blow moulding. J. Appl. Polym. Sci. 103 (1), 564–573. https://doi.org/10.1002/app.25116.

Hieber, C.A., 1995. Correlations for the quiescent crystallization kinetics of isotactic polypropylene and poly(ethylene terephthalate). Polymer 36, 1455. https://doi.org/10.1016/0032-3861(95)95925-Q.

Jabarin, S.A., 1984. Orientation studies of poly(ethylene terephthalate). Polym. Eng. Sci. 24, 376–384. https://doi.org/10.1002/pen.760240513.

Jabarin, S.A., 1987. Crystallization kinetics of polyethylene terephthalate. I. Isothermal crystallization from the melt. J. Appl. Polym. Sci. 34 (1), 85–96. https://doi.org/10.1002/app.1987.070340107.

Laschet, G., Spekowius, M., Hopmann, C., 2017. Multiscale simulation to predict microstructure dependent effective elastic properties of an injection molded polypropylene component. Mech. Mater. 105, 123–137. https://doi.org/10.1016/j.mechmat.2016.10.009.

Liu, Z.J., Ouyang, J., Zhou, W., Wang, X.D., 2015. Numerical simulation of the polymer crystallization during cooling stage by using level set method. Comput. Mater. Sci. 97, 245–253. https://doi.org/10.1016/j.commatsci.2014.10.038.

Lu, X.X., Detrez, F., Roland, S., 2019. Numerical study of the relationship between the spherulitic microstructure and isothermal crystallization kinetics. Part I. 2-D analyses. Polymer 179. https://doi.org/10.1016/j.polymer.2019.121642.

Luo, Y.M., Chevalier, L., Monteiro, E., Utheza, F., 2021. Numerical simulation of self heating during stretch blow moulding of PET: viscohyperelastic modelling versus experimental results. Int. J. Material Form. 14, 703–714. https://doi.org/10.1007/s12289-020-01565-w.

Mandelkern, L., 2004. Crystallization of Polymers, vol. 2. Cambridge University Press.

La Mantia, F.P., Botta, L., Morreale, M., Scaffaro, R., 2012. Effect of small amounts of poly(lactic acid) on the recycling of poly(ethylene terephthalate) bottles. Polym. Degrad. Stabil. 97, 21–24. https://doi.org/10.1016/j.polymdegradstab.2011.10.017.

Medellin-Rodriguez, F.J., Lopez-Guillen, R., Waldo-Mendoza, M.A., 2000. Solid-state polymerization and bulk crystallization behavior of poly(ethylene terephthalate) (PET). J. Appl. Polym. Sci. 75–78. https://doi.org/10.1002/(SICI)1097-4628(20000103)75:1<78::AID-APP9>3.0.CO;2-E.

Menary, G.H., Tan, C.W., Harkin-Jones, E.M.A., Armstrong, C.G., Martin, P.J., 2012. Biaxial deformation of PET at conditions applicable to the stretch blow molding process. Polym. Eng. Sci. 52 (3), 671–688. https://doi.org/10.1002/pen.22134.

Michaeli, W., Hopmann, C., Bobzin, K., Arping, T., Baranowski, T., Heesel, B., Laschet, G., Schläfer, T., Oete, M., 2012. Development of an integrative simulation method to predict the microstructural influence on the mechanical behaviour of semi-crystalline thermoplastic parts. Int. J. Mater. Res. 103 (1), 120–130. https://doi.org/10.3139/146.110628.

Micheletti, A., Burger, M., 2001. Stochastic and deterministic simulation of nonisothermal crystallization of polymers. J. Math. Chem. 30 (2), 169–193. https://doi.org/10.1023/A:1017923703579.

Milton, G., 2002. *The Theory Of Composites* (Cambridge Monographs on Applied and Computational Mathematics). Cambridge University Press, Cambridge. https://doi.org/10.1017/CBO9780511613357.

Mirkhalaf, M., van Dommelen, J.A., Govaert, L.E., Furmanski, J., Geers, M.G., 2019. Micromechanical modeling of anisotropic behavior of oriented semicrystalline polymers. J. Polym. Sci. B Polym. Phys. 57 (7), 378–391. https://doi.org/10.1002/polb.24791.

Molnar, J., Sepsi, Ö., Gaal, B., Zuba, Z., Dobrzyńska-Mizera, M., Menyárd, A., 2021. Probabilistic numerical simulation for predicting spherulitic morphology from calorimetric crystallization conversion curves: an isothermal case. Mater. Des. 212, 110245 https://doi.org/10.1016/j.matdes.2021.110245.

Nakamura, K., Katayama, K., Amano, T., 1973. Some aspects of non-isothermal crystallization of polymers. II. Consideration of the isokinetic condition. J. Appl. Polym. Sci. 17, 1031–1041. https://doi.org/10.1002/app.1973.070170404.

Nikolov, S., Doghri, I., Pierard, O., Zealouk, L., Goldberg, A., 2002. Multi-scale constitutive modeling of the small deformations of semi-crystalline polymers. J. Mech. Phys. Solid. 50 (11), 2275–2302. https://doi.org/10.1016/S0022-5096(02)00036-4.

Oktay, H.E., Gürses, E., 2015. Modeling of spherulite microstructures in semicrystalline polymers. Mech. Mater. 90, 83–101. https://doi.org/10.1016/j.mechmat.2015.04.010.

Pedoto, G., Grandidier, J.-C., Vinet, A., 2021. Characterization and modelling of the PEKK thermomechanical and creep behavior above the glass transition temperature. Mech. Mater. 166, 104189 https://doi.org/10.1016/j.mechmat.2021.104189.

Piorkowska, E., Rutledge, G.C. (Eds.), 2013. Handbook of Polymer Crystallization. John Wiley & Sons.

Raabe, D., 2004. Mesoscale simulation of spherulite growth during polymer crystallization by use of a cellular automaton. Acta Mater. 52 (9), 2653–2664. https://doi.org/10.1016/j.actamat.2004.02.013.

Raabe, D., Godara, A., 2005. Mesoscale simulation of the kinetics and topology of spherulite growth during crystallization of isotactic polypropylene (iPP) by using a cellular automaton Model. Simul. Mater. Sci. Eng. 13 (5), 733. https://doi.org/10.1088/0965-0393/13/5/007.

Regrain, C., Laiarinandrasana, L., Toillon, S., Saï, K., 2009. Multi-mechanism models for semi-crystalline polymer: constitutive relations and finite element implementation. Int. J. Plast. 25 (7), 1253–1279. https://doi.org/10.1016/j.ijplas.2008.09.010.

Reiter, G., Sommer, J.-U., 2003. Polymer Crystallization: Obervations, Concepts and Interpretations, vol. 606. Springer Science & Business Media. https://doi.org/10.1007/3-540-45851-4.

Schmidt, F.M., Agassant, J.F., Bellet, M., 1998. Experimental study and numerical simulation of the injection stretch/blow moulding process. Polym. Eng. Sci. 38 (9), 1399–1412. https://doi.org/10.1002/pen.10310.

Spekowius, M., Spina, R., Hopmann, C., 2016. Mesoscale simulation of the solidification process in injection moulded parts. J. Polym. Eng. 36 (6), 563–573. https://doi.org/10.1515/polyeng-2014-0223.

Spina, R., Spekowius, M., Dahlmann, R., Hopmann, C., 2014. Analysis of polymer crystallization and residual stresses in injection molded parts. Int. J. Precis. Eng. Manuf. 15 (1), 89–96. https://doi.org/10.1007/s12541-013-0309-2.

Spina, R., Spekowius, M., Hopmann, C., 2016. Multiphysics simulation of thermoplastic polymer crystallization. Mater. Des. 95, 455–469. https://doi.org/10.1016/j.matdes.2016.01.123.

Tant, M.R., Culberson, W.T., 1993. Effect of molecular weight on spherulite growth rate of poly(ethylene terephthalate) via real-time small angle light scattering. Polym. Eng. Sci. 33 (17), 1152–1156. https://doi.org/10.1002/pen.760331709.

Teixeira-Pinto, J., Nadot-Martin, C., Touchard, F., Gueguen, M., Castagnet, S., 2016. Towards the size estimation of a representative elementary domain in semi-crystalline polymers. Mech. Mater. 95, 116–124. https://doi.org/10.1016/j.mechmat.2016.01.003.

Thomas, C., Seguela, R., Detrez, F., Miri, V., Vanmansart, C., 2009. Plastic deformation of spherulitic semi-crystalline polymers: an in situ AFM study of polybutene under tensile drawing. Polymer 50 (Issue 15), 3714–3723. https://doi.org/10.1016/j.polymer.2009.06.023.

Thompson, A., Woods, D., 1955. Density of amorphous polyethylene terephthalate. Nature 176, 78–79. https://doi.org/10.1038/176078b.

Torquato, S., 2002. Random Heterogeneous Materials: Microstructure and Macroscopic Properties. Springer, New York. https://doi.org/10.1007/978-1-4757-6355-3.

Wang, X.-D., Jie, O., Jin, S., Wen, Z., 2013. A phase-field model for simulating various spherulite morphologies of semi-crystalline polymers Chin. Phys. B 22 (10), 106103. https://doi.org/10.1088/1674-1056/22/10/106103.

Yan, Z., Guo, Q., Zaïri, F., Zaoui, A., Jiang, Q., Liu, X., 2021. Continuum-based modeling large-strain plastic deformation of semi-crystalline polyethylene systems: implication of texturing and amorphicity. Mech. Mater. 162, 104060 https://doi.org/10.1016/j.mechmat.2021.104060.

Yvonnet, J., 2019. Computational Homogenization of Heterogeneous Materials with Finite Elements, vol. 258. Springer International Publishing. https://doi.org/10.1007/978-3-030-18383-7.